Current Applied Physics 66 (2024) 60–65

Contents lists available at ScienceDirect

Current Applied Physics

journal homepage: www.elsevier.com/locate/cap

Fast growth of large-sized organic single crystals via spin coating

Hyewon Shim [1], Jun-Ho Park [1], Shinyoung Choi, Cheol-Joo Kim [*]

Department of Chemical Engineering, Pohang University of Science and Technology (POSTECH), Pohang, 37673, Republic of Korea

ARTICLE INFO

Keywords:
Organic small molecule
Single crystal
Spin-coating
Charge-transfer complex
TCNQ
TTF

ABSTRACT

Spin-coating stands out as one of the fastest and simplest processes for material solidification. While it is commonly employed for producing polycrystalline thin films, recent endeavors have explored its potential for epitaxial growth, albeit primarily limited to inorganic materials. In this study, we demonstrate the spin-coating method enabling the rapid growth of large-sized organic single crystals (OSCs). Within 2 h, we successfully obtained OSCs with controlled lateral sizes of up to 2 mm, which conventionally takes several weeks using slow solvent evaporation. Raman mapping and UV–Vis absorption measurements confirmed the growths of the OSCs. We propose the growth mechanism by using the supersaturated dynamic fluid model. Furthermore, we demonstrate the device integration of these OSCs for charge-transfer complex channel, revealing ambipolar behavior during gate sweep. This innovative OSCs production method has the potential to advance the various field of science and electronics, traditionally hindered by the scarcity of adequately sized OSCs.

1. Introduction

Organic single crystals (OSCs) have played a pivotal role in driving recent advancements in the fields of organic electronics and optoelectronics [1–4]. The innovation of organic conductors and superconductors has been developed based on the OSCs charge transfer complexes, which still remains a critical issue in current physics and electronics [3,5–8]. The recent advancement of low-dimensional halide perovskite light-emitting diodes also stems from luminescence measurements of their OSCs phases, providing insights into their electron-phonon coupling effects [4,9–11]. The advantage of OSCs research, in comparison to thin-film studies, lies in the highly ordered molecular structure [12,13], negligible defect density [14], and the ability to investigate interface properties with tunable atomic stacking arrangements [6,7]. Consequently, OSCs have found widespread applications across various research areas, and hold potential for further exploration if easier fabrication processes, akin to thin-film methods, are developed.

However, the current fabrication processes for OSCs have been notoriously challenging in meeting the demand. Typically, solution-based methods, such as evaporation or cooling techniques, require several weeks to achieve the desired crystal size at least a few hundred micrometers [6,15]. Vapor-based methods require a specialized vacuum-based setup system which limits their widespread use [16], and the optimization process for their crystal growth is highly sensitive to various factors including furnace temperature gradient, flow rate or humidity [17,18]. This is why most organic research still relies on polycrystalline thin-films due to their easy accessibility and rapid production benefits, despite the well-known advantages of the single-crystalline cases.

Several efforts have been undertaken to enhance the accessibility and production efficiency of OSCs fabrication. One of the most well-known efforts are solution shearing methods, including blade-coating [19,20] and dip-coating [21]. These methods utilize a constant speed and direction of the precursor fluid to induce kinetically favorable conditions for fast OSCs formation. One shortcoming is that these methods also require the setup of a moving substrate using a constant-speed motor with intricate optimization. To make this approach more accessible for a broader range of research areas, much simpler methods that do not require specialized machine setups should be explored.

The spin-coating method has been one of the simplest approaches for various solid-state fabrication processes but has primarily been restricted to polycrystalline thin-film fabrication. Recently, it was reported that epitaxial growth was possible using the spin-coating process [22]. However, this research primarily focuses on inorganic materials, readily accessible through various existing processes. Moreover, it is necessary to address the transfer process of the fabricated single crystals to other substrates, which is essential for a wide range of applications,

* Corresponding author.
E-mail address: kimcj@postech.ac.kr (C.-J. Kim).
[1] H.S and J.P contributed equally to this work.

https://doi.org/10.1016/j.cap.2024.06.016
Received 8 October 2023; Received in revised form 25 June 2024; Accepted 25 June 2024
Available online 29 June 2024

including desired characterizations or device demonstrations.

Here we demonstrate that OSCs can be readily fabricated using a one-step spin-coating process by introducing a controlled environmental chamber. By taking tetracyanoquinodimethane (TCNQ) and tetrathiafulvalene (TTF) as representative examples, we have obtained crystals with controllable lateral sizes of up to 2000 μm within 2 h. The resultant OSCs exhibit the optical absorption and Raman spectra, presenting the formations of high-quality single crystals. Charge transfer complex planes defined on the OSCs display conductive ambipolar behavior with multiple current amplifications at applied gate voltage. This straightforward and rapid process offers significant potential for a wide range of research areas, eliminating the need for specialized setups and lengthy fabrication times.

2. Experimental section

2.1. OSCs fabrication

For the fabrication of TCNQ OSCs, 0.01 g of TCNQ powder (purity >99.0 %, product #: T3034, TCI) was mixed with 4 mL of acetonitrile (purity >99.8 %, product #: A0130, Samchun). For TTF OSCs, 0.01 g of TTF powder (purity >99.0 %, product #: T3380, TCI) was mixed with 4 mL of hexane (purity >95 %, product #: H0112, Samchun).

In the spin-coating process, an octagonal magnetic bar (length × diameter = 22 × 8 mm^2) was placed in the center of a beaker (with spout, diameter × height = 50 × 30 mm^2) previously filled with solvent (acetonitrile or hexane) to a depth of approximately 3 mm. A 1 × 1 cm^2 silicon wafer was attached to the magnetic bar using PVA glue. A 1.5 × 1.5 cm^2 square substrate (fused silica or silicon) was then attached to the silicon wafer using carbon tape. Subsequently, the beaker with the magnetic bar was placed in the center of a stirrer (model: MSH-20 A, Daihan Scientific). Next, 30 μL of the prepared TCNQ or TTF solution was dropped onto the substrate. A watch glass (diameter = 60 mm) was placed with the concave side up, and the stirring speed was adjusted to the desired speed range (100–300 rpm). After complete solvent evaporation on the substrate, which took less than 2 h, the target substrate was detached for further experiments.

2.2. Optical characterization

Local UV–vis absorption data was obtained using a home-built hyperspectral imaging system [23]. Variable-wavelength illumination was achieved by utilizing light emitted by a Xenon lamp and passing it through a monochromator. Raman spectrum and mapping image was obtained using a confocal microscope in a reflective configuration (model: Alpha300RS, Witec) with a 532 nm wavelength laser used for excitation.

2.3. OSCs transfer process & device characterization

To transfer the OSCs onto another substrate, the fabricated OSCs were attached by thermal release tape and subsequently exfoliated. Then, the OSCs were re-attached to the target substrate and annealed at 130 °C to facilitate release. The device was constructed on a 300 nm SiO_2/Si substrate through the following steps: Initially, gold (Au) was thermally evaporated onto the SiO_2 surface via source/drain-patterned shadow masks. The OSCs were then carefully transferred between the source and drain electrodes, with alignment aided by an optical microscope. For the vapor deposition of TTF onto TCNQ OSCs, the entire device was placed in a Petri dish together with TTF powder for a period of one day at room temperature. Current-voltage and gate sweep data were measured using a probe station within a dark shield box (model: MST5500B, MS TECH).

3. Results and discussion

The schematic illustration of the OSCs fabrication process is presented in Fig. 1(a). Initially, the precursor solution was deposited onto a square substrate, followed by spin-coating in a solvent-moistened environment to regulate the solution evaporation rate. After complete drying of the solution, which occurred within 2 h, OSCs were fabricated at the corners of the square substrates, observed in optical image (Fig. S1). Fig. 1(b) and (c) show optical images of the fabricated representative p-type OSCs, tetracyanoquinodimethane (TCNQ), and n-type OSCs, tetrathiafulvalene (TTF), obtained at different spin-coating rotational speeds. As shown in the images, TCNQ crystals exhibited an expected rhombic shape, while TTF crystals took on a rod-like form. It is noteworthy that the lateral sizes of OSCs can be broadly controlled by varying the spin-coating rpm speed. The differing colors of individual crystals are likely due to light interference phenomena, as our observations indicate a close relationship between optical color and OSCs thickness (Fig. S2).

We achieved the largest TCNQ OSCs, with sizes of up to 2000 μm, as shown in Fig. 2(a). The color, which remains yellow as in the precursor, indicates negligible interference due to sufficient thickness. The OSCs' absorption spectrum was confirmed through local hyperspectral measurements, as depicted in Fig. 2(b). The peak position of the absorption wavenumber spectrum (30 kK) closely matched reference data [24]. Notably, this peak position corresponds to intermolecular transitions, distinctly separate from the intramolecular transition region (25 cm^{-1}) observed in solution-phase absorption [24]. Therefore, this clear intermolecular transition peak without any intramolecular transition peak attests to the highly crystalline nature of our spin-coating-fabricated OSCs. The tilt-angle SEM image (Fig. 1(c)) reveals that the OSCs exhibit distinct sharp-edged morphology, clearly distinguishing them from polycrystalline thin-film structures. The height AFM image show that the crystal has a constant thickness of about 0.75 μm and there is no sign of aggregation (Fig. S3). The Raman spectrum, displayed in Fig. 2(d), closely matches prior reports [25]. It is worth noting that the C–CN stretch peak position (1445 cm^{-1}) signifies their intrinsic p-type states in comparison to their n-doping states [26]. Fig. 2(e) presents the Raman mapping image of the TCNQ OSCs, illustrating a continuous plate-like structure without notable defective or impurity related states. Polarization-dependent fluorescent optical imaging is also taken on the as-grown sample as a function of relative in-plane orientations of the sample with respect to the linearly polarized excitation light. The images (Fig. S4(a)) show uniform intensities across the whole sample area, and the polarization angle-dependent intensities (Fig. S4(b)) exhibit the monoclinic symmetry, matched with a TCNQ crystal, and the interaxial angle between the two high-intensity angles is close to ~95°, close to the interaxial (or monoclinic) angle of 98.54° for TCNQ crystal [27]. Our optical imaging and spectroscopic data collectively indicate the well-defined crystalline nature of the OSCs, despite their fabrication solely through a simple spin-coating process within 2 h.

To elucidate how the straightforward spin-coating process produces high-quality organic single crystals (OSCs), we propose a fabrication mechanism based on the model of a supersaturated dynamic fluid. Both convective fluid motion and solvent evaporation are important for managing the fast growth of large crystals in our process. In solution-based growth, the key to obtaining large crystals is to keep the concentration of soluble monomers below the critical concentration during growth. This suppression of additional nucleation allows growth to continue spontaneously from pre-existing seeds [28]. Although an extremely low concentration of solute and a negligible evaporation rate for the solvent could effectively suppress nucleation, the growth rate of crystals would be very low.

Meanwhile, spin coating introduces continuous outward convective fluid motion [29], as depicted in Fig. 3(b), maintaining a low concentration at the outer region of the growth substrate. We note that heterogeneous nucleation is promoted at the interior surface by solvent

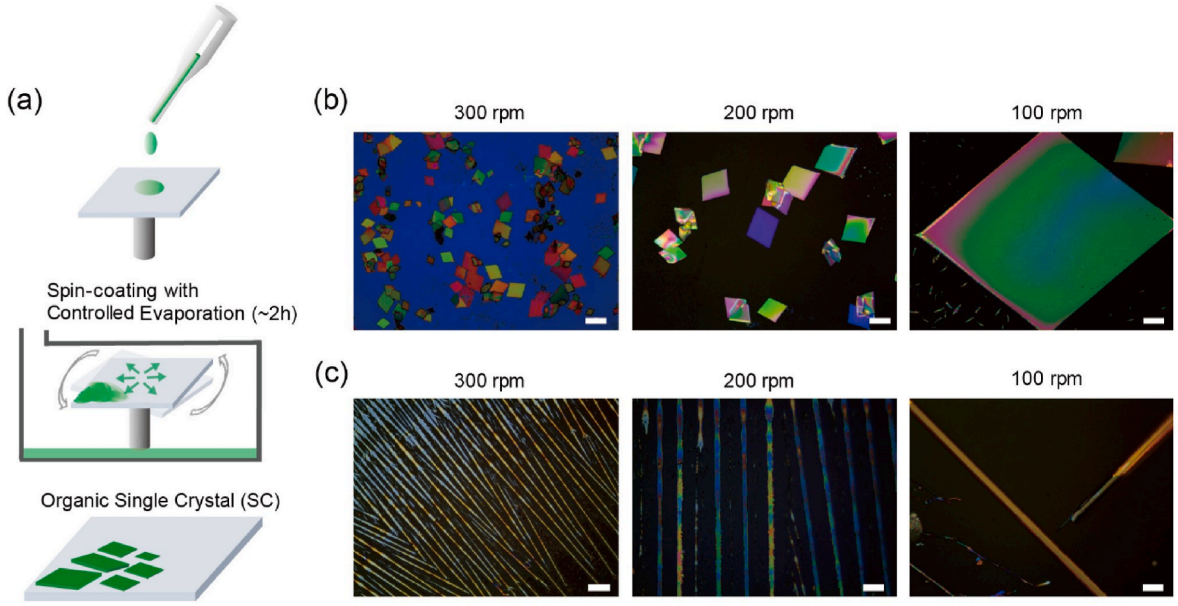

Fig. 1. (a) Schematic representation of the spin-coating-based OSCs fabrication process. (b) TCNQ OSCs and (c) TTF OSCs fabricated at different spin-coating rotational speeds, including 300, 200, and 100 rpm. Scale bar for all images in (b) and (c): 20 μm.

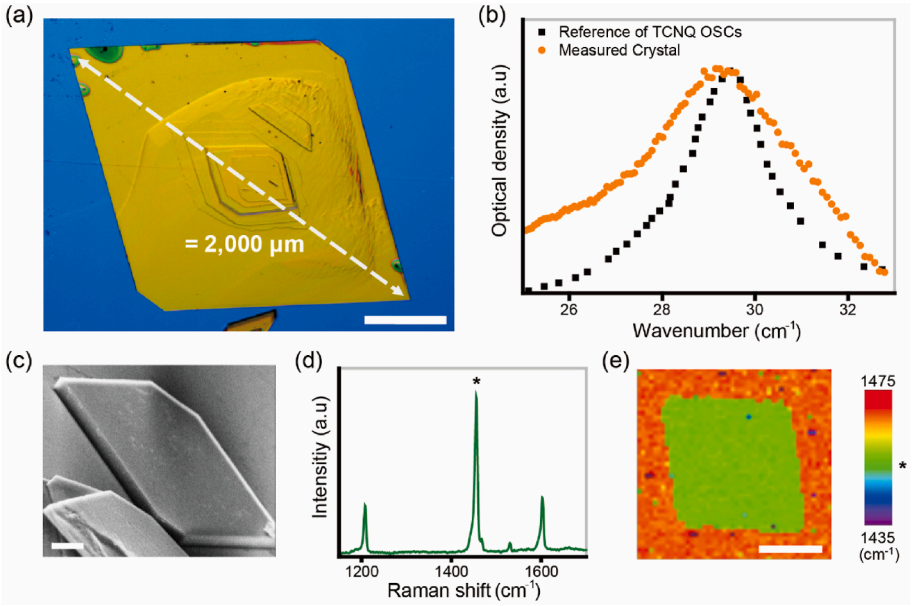

Fig. 2. (a) Fabricated TCNQ OSCs with the largest lateral size as 2000 μm. (b) Micro-spot absorption spectrum of TCNQ OSCs together with reference data [24]. (c) SEM image at a 70° tilt angle of TCNQ OSCs. (d) Raman spectrum and (e) Raman mapping image of TCNQ OSCs. Scale bar for (a): 500 μm. Scale bar for (c) and (e): 20 μm.

extraction outward with a high fluid velocity [30]. Therefore, mainly the solvent can be effectively provided at the outer part during spin coating, maintaining a steady concentration. We found that complete evaporation took up to 2 h at the outer part, resulting in large crystals through controlled growth. We note that the growth rate is still much faster compared to conventional methods, where several tens of hours or days are required to grow large organic single crystals. This faster growth is attributed to the effective separation of solute and solvent by spin coating, which maintains a low monomer concentration at the outer region even with a relatively fast evaporation rate. Additionally, we note that our heterogeneous growth on the surface is beneficial for controlling nucleation, as it is limited to two-dimensional space. Therefore, this method can be useful for obtaining individual large organic crystals.

The fabricated OSCs can be feasibly transferred onto the desired substrates for device fabrications. Our OSCs were originally grown on inorganic amorphous substrates, which were expected to provide weak adhesion. By employing a common transfer method involving thermal release tape [31,32], we successfully transferred the fabricated OSCs to the channel position between the source and drain gold electrodes on a SiO_2/heavily doped Si (Si^{++}) substrate, as depicted in the left scheme of Fig. 4(a). The precise positioning of the OSCs during the transfer process was achieved through meticulous techniques employing an optical microscope [33]. After that, our focus was to investigate the electronic transport behavior of the organic charge transfer complex system by vaporizing TTF onto the surface of TCNQ OSCs, as illustrated in the right scheme of Fig. 4(a) [33]. After TTF vaporization, the transferred TCNQ

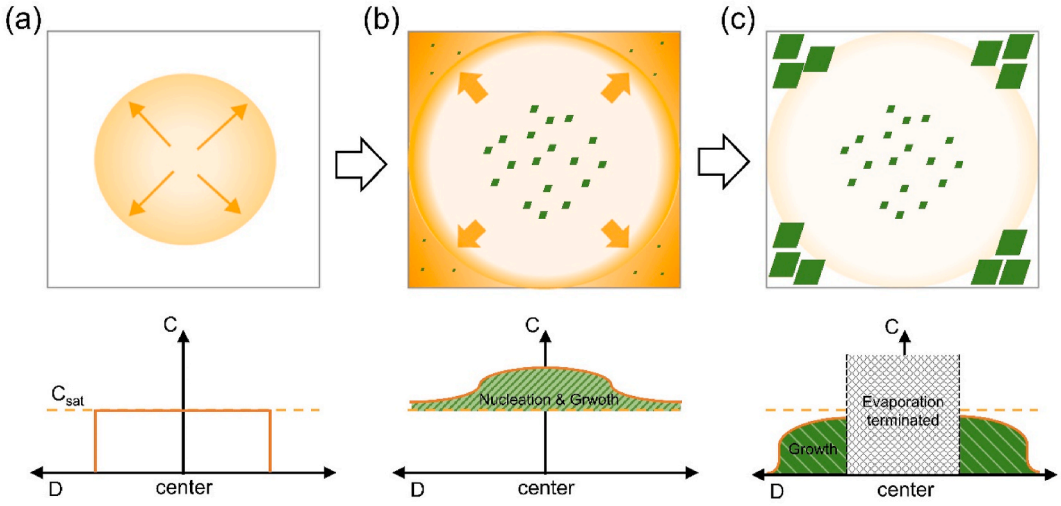

Fig. 3. Proposed mechanism of the spin-coating-based OSCs fabrication process in three steps. (a) (Upper scheme) Initial radial spreading of the solution with (lower graph) rapid saturation in the central region. (b) (Upper scheme) Steady-state solution at the corners with constant radial pressure. (Lower graph) Supersaturated solution forming at the corner region. (c) (Upper scheme) Final OSCs products after complete evaporation with (lower graph) single crystalline solidification.

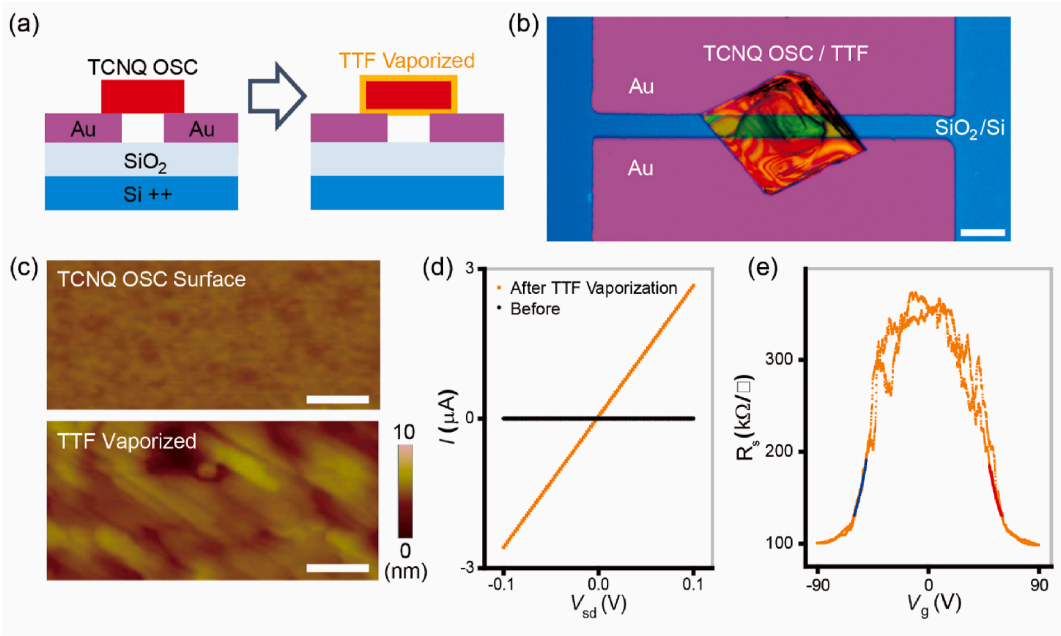

Fig. 4. (a) Schematic of TCNQ OSCs-based device integration (left) with TTF vaporization (right). (b) Optical image of the integrated OSCs devices as illustrated in (a). (c) AFM image of TCNQ OSCs underneath the surface before (upper) and after (lower) TTF vaporization. (d) Source-drain voltage (V_{sd}) - current (I) measurement data before (black) and after (orange) TTF vaporization on TCNQ OSCs. (e) Gate voltage (V_g) – sheet resistance (R_s) measurement data for TTF-vaporized TCNQ OSCs. Scale bar for (b): 100 μm. Scale bar for (c) and (e): 100 nm. (For interpretation of the references to color in this figure legend, the reader is referred to the Web version of this article.)

OSCs exhibited no microscopic shape change in the optical image, as shown in Fig. 4(b). However, nanometer scale morphological changes became evident on the surface of TCNQ OSCs after TTF vaporization. The atomic force microscope (AFM) image of the TCNQ OSCs' underneath surface, depicted in the upper image of Fig. 4(c), revealed that the initial TCNQ OSCs' surface exhibited a flat plane with negligible roughness at the nanometer scale. It's important to note that the OSCs' surface roughness mirrored that of the fabricated substrate, a commercially available SiO_2/Si wafer, which also featured negligible nanoscale roughness. However, the TCNQ OSCs' surface became significantly rough with amplitudes in the tens of nanometers after TTF vaporization, as shown in the lower image of Fig. 4(c). Electrical transport measurements as shown in Fig. 4(d) indicated that TTF vaporization induced a conducting path on the insulating TCNQ OSCs. Consequently, both the AFM and the electrical transport data confirmed the formation of a TTF-TCNQ charge transfer complex on the TCNQ OSCs' surface, as previously reported [34].

In this charge transfer complex system defined on TCNQ OSCs, we applied a gate voltage vertically, and observed ambipolar transport gate sweep behavior, as presented in Fig. 4(e). Intriguingly, the highly conductive pathway exhibited multiple amplifications (4 times) during the gate sweep. This phenomenon is noteworthy because the electronic doping per unit area for the maximum gate voltage could be calculated as only 6×10^{12} cm^{-2}, while the surface density of TTF and TCNQ is

known to be approximately 5×10^{14} cm^{-2} [6], almost two orders of magnitude higher than the injected electron/hole amount. While further investigations are required, we suspect that the electric field-induced strain onto the freestanding soft crystals affect the charge transports along the charge complex surfaces [35].

4. Conclusions

In summary, we have successfully developed an ultrafast and easily accessible method for fabricating high-quality OSCs using a straightforward spin-coating technique, solely by confining solvent humidity. The lateral size of OSCs can be precisely tailored by adjusting the spin-coating speed, achieving dimensions of up to 2000 μm, as confirmed through extensive optical characterizations.

The underlying principle of this rapid OSC fabrication process via spin-coating can be attributed to the generation of a dynamic fluid-induced supersaturated concentration gradient. By employing standard transfer procedures, we integrated these OSCs into the desired device structures. Furthermore, we conducted electrical transport experiments on the source/drain channel-defined organic charge transfer complex system, revealing its ambipolar characteristics under gate voltage sweeps. This simplified and high-speed OSC fabrication process, combined with its transferability, holds immense potential for facilitating research and applications across various fields due to its unparalleled accessibility.

Declaration of competing interest

The authors declare that they have no known competing financial interests or personal relationships that could have appeared to influence the work reported in this paper.

Acknowledgements

This research was supported by the National R&D Program through the National Research Foundation of Korea (NRF) funded by the Ministry of Science and ICT (RS-2023-00234622, 2022M3H4A1A01012718).

Appendix A. Supplementary data

Supplementary data to this article can be found online at https://doi.org/10.1016/j.cap.2024.06.016.

References

[1] C. Wang, H. Dong, L. Jiang, W. Hu, Organic semiconductor crystals, Chem. Soc. Rev. 47 (2018) 422–500, https://doi.org/10.1039/C7CS00490G.
[2] X. Zhang, H. Dong, W. Hu, Organic semiconductor single crystals for electronics and photonics, Adv. Mater. 30 (2018) 1801048, https://doi.org/10.1002/adma.201801048.
[3] H. Jiang, W. Hu, The emergence of organic single-crystal electronics, Angew. Chem. Int. Ed. 59 (2020) 1408–1428, https://doi.org/10.1002/anie.201814439.
[4] W. Chen, Z. Huang, H. Yao, Y. Liu, Y. Zhang, Z. Li, H. Zhou, P. Xiao, T. Chen, H. Sun, J. Huang, Z. Xiao, Highly bright and stable single-crystal perovskite light-emitting diodes, Nat. Photonics (2023), https://doi.org/10.1038/s41566-023-01167-3.
[5] D. Jérome, Organic conductors: from charge density wave TTF–TCNQ to superconducting (TMTSF)2PF6, Chem. Rev. 104 (2004) 5565–5592, https://doi.org/10.1021/cr030652g.
[6] H. Alves, A.S. Molinari, H. Xie, A.F. Morpurgo, Metallic conduction at organic charge-transfer interfaces, Nat. Mater. 7 (2008) 574–580, https://doi.org/10.1038/nmat2205.
[7] I.G. Lezama, M. Nakano, N.A. Minder, Z. Chen, F.V. Di Girolamo, A. Facchetti, A. F. Morpurgo, Single-crystal organic charge-transfer interfaces probed using Schottky-gated heterostructures, Nat. Mater. 11 (2012) 788–794, https://doi.org/10.1038/nmat3383.
[8] K. Xu, H. Sun, T.-P. Ruoko, G. Wang, R. Kroon, N.B. Kolhe, Y. Puttisong, X. Liu, D. Fazzi, K. Shibata, C.-Y. Yang, N. Sun, G. Persson, A.B. Yankovich, E. Olsson, H. Yoshida, W.M. Chen, M. Fahlman, M. Kemerink, S.A. Jenekhe, C. Müller, M. Berggren, S. Fabiano, Ground-state electron transfer in all-polymer donor–acceptor heterojunctions, Nat. Mater. 19 (2020) 738–744, https://doi.org/10.1038/s41563-020-0618-7.
[9] S. Liu, S. Sun, C.K. Gan, A.G. del Águila, Y. Fang, J. Xing, T.T.H. Do, T.J. White, H. Li, W. Huang, Q. Xiong, Manipulating efficient light emission in two-dimensional perovskite crystals by pressure-induced anisotropic deformation, Sci. Adv. 5 (2023) eaav9445, https://doi.org/10.1126/sciadv.aav9445.
[10] B. Zhang, T. Zheng, J. You, C. Ma, Y. Liu, L. Zhang, J. Xi, G. Dong, M. Liu, S. Frank Liu, Electron-phonon coupling suppression by enhanced lattice rigidity in 2D perovskite single crystals for high-performance X-ray detection, Adv. Mater. 35 (2023) 2208875, https://doi.org/10.1002/adma.202208875.
[11] X. Gong, O. Voznyy, A. Jain, W. Liu, R. Sabatini, Z. Piontkowski, G. Walters, G. Bappi, S. Nokhrin, O. Bushuyev, M. Yuan, R. Comin, D. McCamant, S.O. Kelley, E.H. Sargent, Electron–phonon interaction in efficient perovskite blue emitters, Nat. Mater. 17 (2018) 550–556, https://doi.org/10.1038/s41563-018-0081-x.
[12] J.-H. Lee, E.K. Lee, W.-J. Joo, Y. Jang, B.-S. Kim, J.Y. Lim, S.-H. Choi, S.J. Ahn, J. R. Ahn, M.-H. Park, C.-W. Yang, B.L. Choi, S.-W. Hwang, D. Whang, Wafer-scale growth of single-crystal monolayer graphene on reusable hydrogen-terminated germanium (80), Science 344 (2014), https://doi.org/10.1126/science.1252268, 286 LP – 289.
[13] H. Li, C. Fan, W. Fu, H.L. Xin, H. Chen, Solution-grown organic single-crystalline donor–acceptor heterojunctions for photovoltaics, Angew. Chem. Int. Ed. 54 (2015) 956–960, https://doi.org/10.1002/anie.201408882.
[14] J. Siekmann, S. Ravishankar, T. Kirchartz, Apparent defect densities in halide perovskite thin films and single crystals, ACS Energy Lett. 6 (2021) 3244–3251, https://doi.org/10.1021/acsenergylett.1c01449.
[15] M. Yang, Z. Nie, X. Li, R. Wang, Y. Zhao, H. Wang, Advances of metal halide perovskite large-size single crystals in photodetectors: from crystal materials to growth techniques, J. Mater. Chem. C 11 (2023) 5908–5967, https://doi.org/10.1039/D2TC04913A.
[16] H. Jiang, C. Kloc, Single-crystal growth of organic semiconductors, MRS Bull. 38 (2013) 28–33, https://doi.org/10.1557/mrs.2012.308.
[17] X. Zeng, D. Zhang, L. Duan, L. Wang, G. Dong, Y. Qiu, Morphology and fluorescence spectra of rubrene single crystals grown by physical vapor transport, Appl. Surf. Sci. 253 (2007) 6047–6051, https://doi.org/10.1016/j.apsusc.2007.01.008.
[18] A.R. Ullah, A.P. Micolich, J.W. Cochrane, A.R. Hamilton, The effect of temperature and gas flow on the physical vapour growth of mm-scale rubrene crystals for organic FETs, Proc. SPIE (2008) 680005, https://doi.org/10.1117/12.759015.
[19] G. Giri, E. Verploegen, S.C.B. Mannsfeld, S. Atahan-Evrenk, D.H. Kim, S.Y. Lee, H. A. Becerril, A. Aspuru-Guzik, M.F. Toney, Z. Bao, Tuning charge transport in solution-sheared organic semiconductors using lattice strain, Nature 480 (2011) 504–508, https://doi.org/10.1038/nature10683.
[20] A. Yamamura, S. Watanabe, M. Uno, M. Mitani, C. Mitsui, J. Tsurumi, N. Isahaya, Y. Kanaoka, T. Okamoto, J. Takeya, Wafer-scale, layer-controlled organic single crystals for high-speed circuit operation, Sci. Adv. 4 (2023) eaao5758, https://doi.org/10.1126/sciadv.aao5758.
[21] J. Jang, S. Nam, K. Im, J. Hur, S.N. Cha, J. Kim, H. Bin Son, H. Suh, M.A. Loth, J. E. Anthony, J.-J. Park, C.E. Park, J.M. Kim, K. Kim, Highly crystalline soluble acene crystal arrays for organic transistors: mechanism of crystal growth during dip-coating, Adv. Funct. Mater. 22 (2012) 1005–1014, https://doi.org/10.1002/adfm.201102284.
[22] M.V. Kelso, N.K. Mahenderkar, Q. Chen, J.Z. Tubbesing, J.A. Switzer, Spin coating epitaxial films (80), Science 364 (2019) 166–169, https://doi.org/10.1126/science.aaw6184.
[23] S. Choi, N.N. Nguyen, Y. Lee, S.-J. Yang, K. Kim, K. Cho, C.-J. Kim, Nanoscale molecular building blocks for layer-by-layer assembly, Adv. Mater. Interfac. 7 (2020) 2000522, https://doi.org/10.1002/admi.202000522.
[24] S. Hiroma, H. Kuroda, H. Akamatu, Polarized absorption spectra of the TCNQ crystal, Bull. Chem. Soc. Jpn. 43 (1970) 3626–3627, https://doi.org/10.1246/bcsj.43.3626.
[25] P.G. Gucciardi, S. Trusso, C. Vasi, S. Patanè, M. Allegrini, Nano-Raman imaging of Cu–TCNQ clusters in TCNQ thin films by scanning near-field optical microscopy, Phys. Chem. Chem. Phys. 4 (2002) 2747–2753, https://doi.org/10.1039/B110475F.
[26] S. Matsuzaki, R. Kuwata, K. Toyoda, Raman spectra of conducting TCNQ salts; Estimation of the degree of charge transfer from vibrational frequencies, Solid State Commun. 33 (1980) 403–405, https://doi.org/10.1016/0038-1098(80)90429-9.
[27] J.W. Rohleder, T. Luty, The “oriented gas model” and its application to the infrared spectroscopy of molecular crystals, Mol. Cryst. 5 (1968) 145–163, https://doi.org/10.1080/15421406808082936.
[28] L. Zeng, S. Chen, K. Forberich, C.J. Brabec, Y. Mai, F. Guo, Controlling the crystallization dynamics of photovoltaic perovskite layers on larger-area coatings, Energy Environ. Sci. 13 (2020) 4666–4690, https://doi.org/10.1039/D0EE02575E.
[29] D.P. Birnie III, A model for drying control cosolvent selection for spin-coating uniformity: the thin film limit, Langmuir 29 (2013) 9072–9078, https://doi.org/10.1021/la401106z.
[30] J.Y. Na, B. Kang, S.G. Lee, K. Cho, Y.D. Park, Surface-mediated solidification of a semiconducting polymer during time-controlled spin-coating, ACS Appl. Mater. Interfaces 9 (2017) 9871–9879, https://doi.org/10.1021/acsami.6b11737.
[31] J.-H. Park, Y. Reo, J.-H. Jung, T. Kim, T. Park, Y.-Y. Noh, C.-J. Kim, Reduction of Hole Carriers by van der Waals Contact for Enhanced Photoluminescence Quantum Yield in Two-Dimensional Tin Halide Perovskite, ACS Energy Lett. 8 (2023) 3536–3544, https://doi.org/10.1021/acsenergylett.3c01195.

[32] J.-H. Park, S.-J. Yang, C.-W. Choi, S.-Y. Choi, C.-J. Kim, Pristine graphene insertion at the metal/semiconductor interface to minimize metal-induced gap states, ACS Appl. Mater. Interfaces 13 (2021) 22828–22835, https://doi.org/10.1021/acsami.1c03299.
[33] S.-J. Yang, J.-H. Jung, E. Lee, E. Han, M.-Y. Choi, D. Jung, S. Choi, J.-H. Park, D. Oh, S. Noh, K.-J. Kim, P.Y. Huang, C.-C. Hwang, C.-J. Kim, Wafer-scale programmed assembly of one-atom-thick crystals, Nano Lett. 22 (2022) 1518–1524, https://doi.org/10.1021/acs.nanolett.1c04139.
[34] T. Mathis, K. Mattenberger, P. Moll, B. Batlogg, Tetrathiofulvalene and tetracyanoquinodimethane crystals: conducting surface versus interface, Appl. Phys. Lett. 101 (2012) 23302, https://doi.org/10.1063/1.4731244.
[35] Y. Kawasugi, K. Seki, S. Tajima, J. Pu, T. Takenobu, S. Yunoki, H.M. Yamamoto, R. Kato, Two-dimensional ground-state mapping of a Mott-Hubbard system in a flexible field-effect device, Sci. Adv. 5 (2023) eaav7282, https://doi.org/10.1126/sciadv.aav7282.